Linking Metastatic Potential and Viscoelastic Properties of Breast Cancer Spheroids via Dynamic Compression and Relaxation in Microfluidics

Tavasso, Margherita; Bordoloi, Ankur D.; Tanré, Elsa; Dekker, Sanne A.H.; Garbin, Valeria; Boukany, Pouyan E.

DOI
10.1002/adhm.202402715

Publication date
2024

Document Version
Final published version

Published in
Advanced Healthcare Materials

ADVANCED HEALTHCARE MATERIALS
www.advhealthmat.de

Linking Metastatic Potential and Viscoelastic Properties of Breast Cancer Spheroids via Dynamic Compression and Relaxation in Microfluidics

Margherita Tavasso, Ankur D. Bordoloi, Elsa Tanré, Sanne A. H. Dekker, Valeria Garbin, and Pouyan E. Boukany**

The growth and invasion of solid tumors are associated with changes in their viscoelastic properties, influenced by both internal cellular factors and physical forces in the tumor microenvironment. Due to the lack of a comprehensive investigation of tumor tissue viscoelasticity, the relationship between such physical properties and cancer malignancy remains poorly understood. Here, the viscoelastic properties of breast cancer spheroids, 3D (in vitro) tumor models, are studied in relation to their metastatic potentials by imposing controlled, dynamic compression within a microfluidic constriction, and subsequently monitoring the relaxation of the imposed deformation. By adopting a modified Maxwell model to extract viscoelastic properties from the compression data, the benign (MCF-10A) spheroids are found to have higher bulk elastic modulus and viscosity compared to malignant spheroids (MCF-7 and MDA-MB-231). The relaxation is characterized by two timescales, captured by a double exponential fitting function, which reveals a similar fast rebound for MCF-7 and MCF-10A. Both the malignant spheroids exhibit similar long-term relaxation and display residual deformation. However, they differ significantly in morphology, particularly in intercellular movements. These differences between malignant spheroids are demonstrated to be linked to their cytoskeletal organization, by microscopic imaging of F-actin within the spheroids, together with cell-cell adhesion strength.

1. Introduction

The progression and invasion of solid tumors involve a complex interplay between tumor cells and their surrounding environment including blood and lymph vessels, immune cells, fibroblasts and extracellular matrix (ECM).[1,2] From a physical perspective, such interactions translate into solid stress (compressive and tensile forces applied by non-fluidic elements of the tumor environment) and interstitial fluid pressure, arising from tumor growth in confined spaces, ECM stiffening and remodeling, leaky blood vessels and altered lymphatic drainage system.[3] The mechanical properties of tissues, such as elasticity and viscosity, are significantly influenced by these cues, and instigate biochemical changes, which ultimately facilitate metastasis.[4,5]

The viscoelastic characterization of tumor cells has become a key indicator of tumor development and metastasis.[6] Nanomechanical analysis, performed using atomic force microscopy (AFM) of individual metastatic cells (from breast, lung and pancreatic cancer) in pleural fluids of patients showed that cancer cells are softer than their healthy counterparts.[7] This cell softening serves as a biomechanical adaptation to facilitate cancer invasion.[8] Several studies highlighted how confinement and compression can alter the intracellular structure of single cancer cells, linking their mechanical properties to their metastatic potential at the single-cell level. Malignant breast cancer cells traveling through microchannels that mimic blood vessels demonstrated to exhibit greater deformability compared to benign cell types.[9,10] Additionally, invasive breast cancer cells showed residual irreversible deformations after squeezing through a tight constricted microchannel under flow conditions, attributed to cytoskeleton rearrangements.[11] Furthermore, nuclear envelope rupture and DNA damage occurred in several cancer cell lines during confined migration through narrow spaces and external compression.[12]

At the tissue level, tumor cells are densely packed, held together by cell-cell junctions and surrounded by denser extracellular matrix, resulting in a stiffer tumor tissue compared to the

M. Tavasso, A. D. Bordoloi, S. A. H. Dekker, V. Garbin, P. E. Boukany
Department of Chemical Engineering
Delft University of Technology
Delft 2629 HZ, The Netherlands
E-mail: a.d.bordoloi@tudelft.nl; p.e.boukany@tudelft.nl
E. Tanré
École Polytechnique
Institut Polytechnique de Paris
Palaiseau 91120, France

The ORCID identification number(s) for the author(s) of this article can be found under https://doi.org/10.1002/adhm.202402715

DOI: 10.1002/adhm.202402715

surrounding healthy tissue.[13,14] For this reason, numerous studies investigated how the mechanical properties of the ECM can profoundly alter single and collective cell migration from a primary tumor: the response to different levels of compressive, tensile and elongational stresses can be monitored in in vitro 3D tumor models (spheroids) by tuning the viscoelasticity, stiffness and composition of the surrounding matrix.[15–18] These approaches, however, only analyzed the solid tumor response in static conditions and in relation to the ECM composition,[16] making it difficult to decouple the intrinsic spheroid's viscoelastic properties in response to dynamic external stresses from those of the surrounding ECM. In order to link the biophysical characteristics of spheroids and their metastatic potential in the early stage of metastasis, it is important to investigate these mechanical properties of tumor spheroids independent of the ECM. Solid and interstitial stress vary over a range of 0.21-20 kPa[19,20] depending on the tissue examined and the tumor stage. Real time monitoring of 3D in vitro assays that impose and release controlled stress under biologically relevant conditions can unravel these properties.

Microfluidics provides a powerful platform to explore the viscoelastic properties of cancer spheroids within confined environment, due to its tunable geometries and dimensions.[21] Recent works involved microfluidic devices to study spheroid mechanics via micropipette aspiration (MPA) in a high-throughput manner,[22] or via compressing cellular aggregates in microchannels, to assess viscoelastic properties associated with the cell rearrangement and cell shape within the aggregate.[23,24] Despite the valuable insights on the viscoelastic properties of tumor models gained from these studies, the relationship between the intrinsic viscoelastic characteristics of cancer spheroids and the degree of malignancy remains to be elucidated.

In this work, we establish this link by focusing on spheroids made from one non-tumorigenic epithelial cell line (MCF-10A) and two breast cancer cell lines with increasing metastatic potential(MCF-7 and MDA-MB-231). In a microfluidic chip, the spheroids are subjected to dynamic compression through a narrow constriction channel, with different level of confinement. We quantify the spheroids viscoelastic properties, by fitting the compression data to a modified Maxwell model adapted to the dynamic conditions, from which it is possible to distinguish the benign from the malignant spheroids. Then, we characterized the shape recovery of spheroids after compression during the relaxation process. Notably, comparing the fast and slow relaxation timescales of spheroids allows us to discern different degrees of malignancy, which we demonstrate to be closely associated with spheroid compactness and actin cortex arrangement.

2. Results

2.1. Microfluidic Assay for Dynamic Compression and Relaxation of Breast Cancer Spheroids

We develop a microfluidic assay to investigate the viscoelastic response of breast cancer spheroids subjected to dynamic compression. This assay involves flowing spheroids through a narrow constriction channel connected with a relaxation chamber (see **Figure 1a**). The flow rate is kept constant using a syringe pump. The pump withdraws one spheroid at a time from a suspension at the micropipette loading port, compressing each spheroid through the constriction channel (referred to as the compression stage). After passing through the constriction, the spheroids are released into a wider chamber where they can relax in the absence of flow (referred to as the relaxation stage). The spheroid undergoes maximum compressive strain within the constriction channel, measured by the constriction index $I_c = (D_0 - d_c)/D_0$, defined by the width of the constricting channel d_c, and the equivalent spherical diameter of the spheroid D_0, such that a larger I_c signifies larger maximum strain. We prevent the spheroid from tumbling in the observation plane by maintaining the channel height below D_0 (180 ± 15 µm). We estimate the spheroid deformation during dynamic compression through the axial strain $\epsilon = (D(t) - D_0)/D_0$, where $D(t)$ refers to the axial dimension of the deformed spheroid over time (Figure 1b).

The dynamic compression of the spheroid can be characterized by three distinct phases: tongue aspiration ($t_1 < t \leqslant t_2$), impregnation ($t_2 < t \leqslant t_3$), and maximal compression ($t_3 < t \leqslant t_4$). Figure 1d captures the dynamics of these phases for a representative MCF-7 spheroid with $I_c = 0.63$, demonstrating the corresponding time-wise variations in the (I) pressure difference across the channel (ΔP), (II) velocity of the spheroid (u_s), and (III) its axial strain (ϵ). Immediately after clogging the entrance of the constriction channel ($t = t_1$), the spheroid's velocity drops significantly, accompanied by an increased pressure difference across the channel. This increasing ΔP dynamically compresses the spheroid by initiating a tongue at the leading front that is aspirated through the channel ($t > t_1$). As soon as the spheroid's centroid transits the constriction channel ($t = t_2$), the trailing end rapidly slips into the channel, leading to complete impregnation at $t = t_3$ and a sudden acceleration of the spheroid. During this phase, a rapid growth in axial strain ϵ takes place, reaching its maximum during the time $t_3 < t \leqslant t_4$ as the spheroid flows inside the constriction channel. At $t \geqslant t_4$, the spheroid unclogs and exits from the constriction enabling fluid flow through the channel, with a consequent drop in ΔP and u_s.

We monitor the relaxation of the spheroid for 30 min in the adjacent relaxation chamber. The relaxation monitoring was restricted to 30 min to minimize cell contact with the underlying glass slide and ensure cell viability (details in the Experimental Section). Unlike the constrained relaxation observed in MPA,[25] the spheroids here are allowed to relax freely after exiting the constriction channel. Due to the imaging conditions and the chip design, it is not possible to capture both the constriction channel and the relaxation chamber within the same field of view. This results in a lag time $t_{lag} \approx$ 15-34 s (Figure S1, Supporting Information) between the frames at t_4, where the spheroids experience maximum compression, and the start of the relaxation monitoring (Figure 1c). We quantify the spheroid's morphological relaxation through a deformation parameter (S_r) and the circularity (C_r). Here, $S_r = \frac{a(t)-b(t)}{a(t)+b(t)}$ with a and b being the major and minor axes of the ellipse, respectively, that fits the 2D spheroid boundary (see Figures 1c and 3a)[26–28] (details in the Experimental Section, Data acquisition and analysis). The circularity is quantified as $C_r = (4\pi \cdot \text{Area}/\text{Perimeter}^2)$.

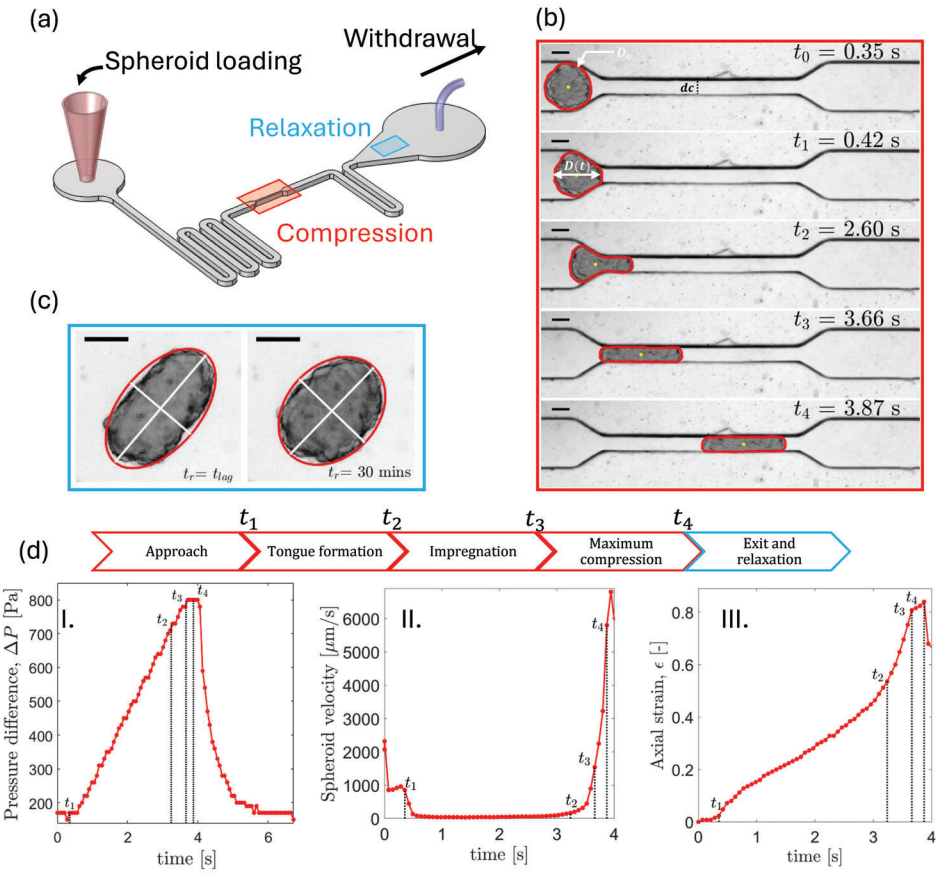

Figure 1. Design and working principle of the microfluidic device for viscoelastic characterization of breast spheroids with different level of malignancy. a) Schematic of the microfluidic chip for spheroids' dynamic compression and relaxation. The rectangles identify the middle constriction (red) and the relaxation chamber (light blue). b) Showcase of MCF-7 ($l_c = 0.63$) spheroid during the compression stage, with emphasis on relevant time points. The equivalent spherical diameter D_0 and the axial dimension over time $D(t)$ are highlighted. The spheroid edge is in red and the centroid in yellow. c) Showcase of the same MCF-7 spheroid during the relaxation stage at recovery time $t_r = t_{lag}$ and 30 min respectively. A red ellipse estimates the spheroid's shape, with the major and minor axes, shown in white, tracked over time for subsequent data analysis. d) Time axis and identification of relevant time points of the compression stage and corresponding evolution of pressure difference across the channel (I), spheroid's velocity (II) and axial strain (III) as function of time. Scale bar of the brightfield images: 100 μm.

2.2. Viscoelastic Response as a Signature of Metastatic Potential in Spheroids Under Compression

To probe the link between viscoelastic properties of spheroids and their cancer malignancy, we measure the axial deformation during the dynamic compression of three different breast cancer spheroids, formed from benign cells (MCF-10A) and from low and high metastatic cells (MCF-7 and MDA-MB-231). **Figure 2**a shows the time evolution of axial strain (ϵ) for three representative spheroids of each phenotype. Notably, the spheroid from the healthy cell line (MCF-10A) exhibits the highest resistance to deformation, followed by MCF-7 and MDA-MB-231, consistent with their increasing metastatic potential (see Movie S1, Supporting Information). The benign spheroid (MCF-10A) demonstrates a significant delay in tongue formation with $t_1 = 68.9$ s, in contrast to the two cancer spheroids (MCF-7 and MDA-MB-231) with $t_1 \approx 0.07$ s (as shown in Figure 2c). This results in an order of magnitude longer entry time ($t_E = t_3 - t_0$) (see Figure 2d), defined as the duration from when the spheroid contacts the entrance of the constriction channel (t_0) until the spheroid has completely entered the middle channel (t_3). We do not observe a statistically significant difference in t_E between the two malignant spheroids (MCF-7 and MDA-MB-231). Once the spheroid is fully inside the constriction channel during maximum compression, it traverses through the channel at nearly the same rate regardless of the cell type.

To estimate the elastic modulus (E) and viscosity (η) of each spheroid based on the evolution of its axial strain under dynamic compression, we adapt the modified Maxwell model to account for the dynamic experimental conditions of our microfluidic assay. The modified Maxwell model was previously applied to MPA techniques to assess the viscoelastic properties of biological drops,[29] and multicellular spheroids.[22,30] The proposed model consists of four elements,[31] as depicted in Figure 2b: the Kelvin–Voigt body is characterized by a spring of elasticity E, accounting for the bulk elasticity of the spheroid, in parallel with a spring of elasticity E^* and a dashpot of viscosity η^*. The latter two describe the initial elastic jump in the strain and the local viscosity respectively. Another dashpot in series characterizes the bulk viscosity η of the spheroid (or aggregate). The governing

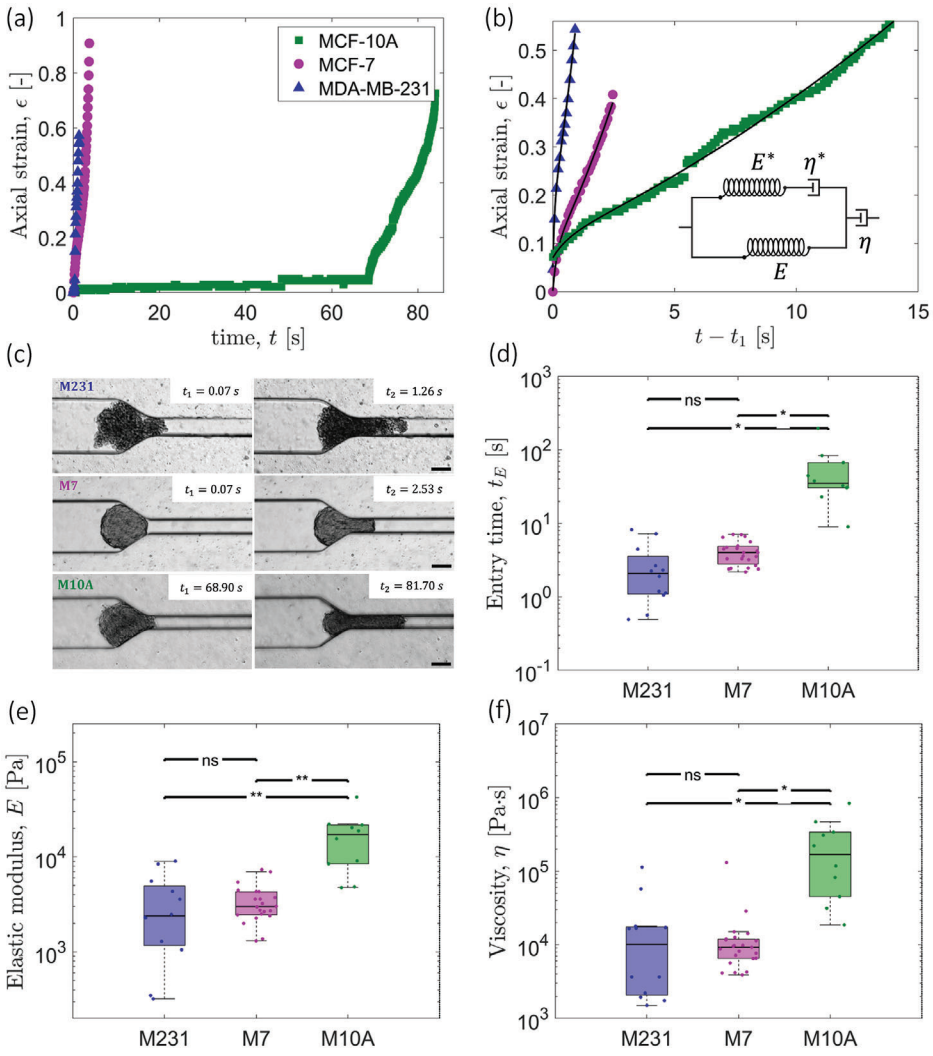

Figure 2. Dynamic compression of spheroid and the Dynamic Modified Maxwell model (D3M) fitting to determine spheroids viscoelastic properties. a) Time-wise evolution of axial strain during spheroid dynamic compression and deformation: the MCF-10A curve shows a delay in the rising of the axial strain, attributed to the longer time needed for tongue formation. b) The strain curves, shifted to the beginning of tongue formation t_1, are fitted with the D3M, the model being illustrated in the inset. c) Brightfield images of MDA-MB-231, MCF-7 and MCF-10A spheroids in the constriction channel: snapshots taken at time t_1 and t_2, showing that the time for MCF-10A spheroids for tongue formation is much longer than the other two malignant spheroids. Scale bar: 100 µm. d) Entry time (t_E) of the three spheroid types for $I_c \geqslant 0.6$. MDA-MB-231 (n=12) and MCF-7 (n=23) spheroids require a shorter time to fully enter the middle constricted channels compared to MCF-10A (n=10). e) and f) Boxplots comparing the spheroids bulk elastic moduli (E) and viscosity (η) for different metastatic potentials and for constriction index $I_c \geqslant 0.6$ (n_{M231}=12), (n_{M7}=23), (n_{M10A}=10). Data = solid line in the boxplot is the sample median. Box edges are first and third quartiles (IQR). Whiskers within 1.5 IQR value. The significance was calculated by a two-tailed t-test: ns = non significant, $p < 0.01$ (**) and $p < 0.05$ (*).

empirical equation describing strain evolution in this system is given by (full derivation in SI):

$$\ddot{\varepsilon} + \frac{\dot{\varepsilon}}{\tau_c} = \left(\frac{1}{E\tau_c} + \frac{1}{\eta}\right)\dot{\sigma} + \frac{1}{\eta\tau_c}\sigma \tag{1}$$

where $\tau_c = \frac{\eta^*(E+E^*)}{EE^*}$ is a characteristic time for the fast elastic jump, determined by the cell-scale viscoelasticity (E^* and η^*).[31] The applied stress σ, due to the pressure difference across the channel, is given by $\sigma(t) = \Delta P(t) = \Delta P_0 + \Delta \dot{P} t$. Here, $\Delta \dot{P}$ is the slope of the linear increment in the pressure (ΔP) against time during tongue formation (see Figure 1d (I)). The integration of Equation (1) yields the generalized equation presented in Equation (2), which we refer to as the dynamic modified Maxwell model (D3M). This model describes strain as a function of the time-dependent pressure difference (linked to the applied stress), and the viscoelastic parameters (E and η) of the spheroid:

$$\varepsilon(t) = \frac{\Delta P_0}{E}\left(1 - \frac{E^*}{E^* + E}e^{-\frac{t}{\tau_c}}\right) + \frac{\Delta P_0 t}{\eta} + \frac{\Delta \dot{P} t}{E} + \frac{\Delta \dot{P} t^2}{2\eta} + \frac{\Delta \dot{P}\eta^*}{E^2}\left(e^{-\frac{t}{\tau_c}} - 1\right) \tag{2}$$

The right-hand side of Equation (2) comprises five terms: the non-linear elastic jump, linear viscous and linear elastic terms, non-linear viscous term, and non-linear viscoelastic term. The analysis reported in Figure S2 (Supporting Information) shows that the last term, with E^2 in the denominator, is negligible. In the limit of a constant ΔP, condition used in earlier studies with micropipette aspiration, we recover the modified Maxwell model equation.[29] Since the D3M considers the pressure to be a linear function of time, the onset time for tongue aspiration (t_1) corresponds to $\Delta P = \Delta P_0$, initial condition of the model. As illustrated in Figure 2b, this D3M model captures the strain evolution curve through the tongue aspiration phase ($t_1 < t \leqslant t_2$) for all three spheroids. The brightfield images in Figure 2c compare the shape of each spheroid phenotype at the beginning (t_1) and the end (t_2) of the tongue aspiration phase. The accuracy of the D3M fit is found to be better than the modified Maxwell model (see Figure S3 and Table S1, Supporting Information), which does not include the time-dependent linear elastic and non-linear viscous components of strain (see Equation 2). The data, as well as the model, shows a more distinct initial jump in ϵ for the more metastatic cell line, MDA-MB-231, which emphasizes the tendency of tumor cells to respond promptly and adapt to the deformations induced by either external forces or confinements. Immediately after the end of aspiration (when the spheroid centroid enters the constriction), the model becomes incapable to capture the sudden increase in strain, likely due to the unaccounted acceleration of the spheroid in the subsequent impregnation phase.

The viscoelastic response observed in Figure 2b is reflected in the parameters (E and η) obtained from fitting the D3M: Figure 2e,f reveal that the benign (MCF-10A) spheroids have higher elastic modulus and viscosity compared to the spheroids made of malignant cells for the constriction index ranges $I_c \geqslant 0.6$. The values of elastic modulus and viscosity are in agreement with previous studies that employed MPA,[22,23] compression tests[32–34] and AFM on breast spheroids,[35] which reported elastic moduli of the order of $\sim 10^2 - 10^3 Pa$ and viscosity reaching values up to $10^5 Pa \cdot s$. The time-scale ($\tau_t = \eta/E$) over which the spheroid transitions from the elastic to the viscous regime during compression[31] is higher for MCF-10A (median $\tau_t = 8.3$ s) compared to MCF-7 (median $\tau = 2.9$ s) and MDA-MB-231 (median $\tau_t = 4.4$ s), suggesting that the benign spheroid transitions more slowly into the viscous regime than the malignant spheroids (see Figure S4, Supporting Information).

We also compare the viscoelastic properties of MCF-7 and MCF-10A spheroids at low and high levels of compression, with $I_c < 0.6$ and $I_c \geqslant 0.6$, respectively (see Figure S5, Supporting Information). Notably, the spheroid viscoelasticity for MCF-10A is I_c-dependent, showing an order of magnitude increase for both E and η as the imposed compression increases ($I_c \geqslant 0.6$), in a similar trend as in single cells observed previously.[36] The effect of the constriction index for MCF-7 spheroids is minimal, with no significant difference in both E and η for lower compression levels, when $I_c \geqslant 0.6$. The experiments with MDA-MB-231 cells are limited only to $I_c \geqslant 0.6$ due to the difficulties in forming smaller, more compact spheroids that would fall within a lower I_c range.

2.3. Relaxation Response and Shape Recovery of Spheroids with Different Metastatic Potentials

To test if the relaxation behavior of the spheroids also bears signatures of metastatic potential, we analyze their subsequent shape recovery in the absence of flow. **Figure 3a** shows representative images of three spheroids at the first ($t = t_{lag}$) and last ($t = 30$ min) captured frames in the relaxation chamber. Figure 3b,c illustrates the typical relaxation of MDA-MB-231, MCF-7 and MCF-10A spheroids through the time-wise evolution in the dimensionless deformation parameter (S_r) and circularity (C_r). For both curves, the starting points correspond to the values of S_r and C_r at the moment of maximum compression at $t = t_4$. This allows for the retrieval of the spheroid status immediately preceding the start of relaxation despite the lag time. After a fast rebound (see inset of Figure 3b), all three spheroids relax slowly and asymptotically toward a plateau (see Movie S2, Supporting Information). In contrast to healthy MCF-10A spheroid, the malignant MCF-7 spheroid continues to relax and does not retrieve its original deformation (S_{r0}) until the end of the experiment (≈ 30 min). This results in a residual deformation ($S_{r\infty} > S_{r0}$) for MCF-7, associated with long time viscous effects. Interestingly, the MDA-MB-231 spheroid shows a different relaxation behavior compared to the other two cell-types. The MDA-MB-231 (with mesenchymal features) spheroid relaxes through rearrangement of constituent cells, such that the final deformation parameter ($S_{r\infty}$) fluctuates significantly among cases and even reduces below its pre-compression value S_{r0} in the example shown in Figure 3b. To quantify the fast and slow relaxation and the subsequent residual deformation of breast spheroids, we employ a double exponential model (DEM) fit to the measured temporal deformation parameter (S_r), given by:

$$S_r(t) = A_1 \exp(-t/\tau_1) + A_2 \exp(-t/\tau_2) + S_{r\infty} \quad (3)$$

The DEM characterizes the multiscale relaxation process via the two time-scales: τ_1 (short) and τ_2 (long), and the residual deformation ($S_{r\infty}$) as fitting parameters. Herein, τ_1 corresponds to the immediate rebound of the spheroid after exiting from the constriction channel, and τ_2 to the subsequent long-term local rearrangements, likely associated with inter-cellular interactions. Both breast cancer single cells and other non-cancerous compressed multicellular aggregates are known to exhibit such double exponential behavior as observed in earlier studies,[32,37–40] based on other techniques like tissue surface tensiometry and AFM. For the spheroids used in our study, the relaxation curves are better captured by the DEM compared to some other fitting models, such as a single exponential and power-law fittings,[41,42] as shown in Figure S6 (Supporting Information).

All three types of spheroids show an early-time fast elastic rebound with τ_1 of the order of ≈ 10 s, indicating an immediate elastic response after exiting the constriction. We find this timescale to be the shortest for the benign spheroid (MCF-10A), followed by progressively longer τ_1 corresponding to malignant spheroids (MCF-7 and MDA-MB-231), as shown in Figure 3d. The statistical difference in τ_1 among the three spheroid is significant only when comparing the benign (MCF-10A) and low-metastatic (MCF-7) spheroids with the highly metastatic

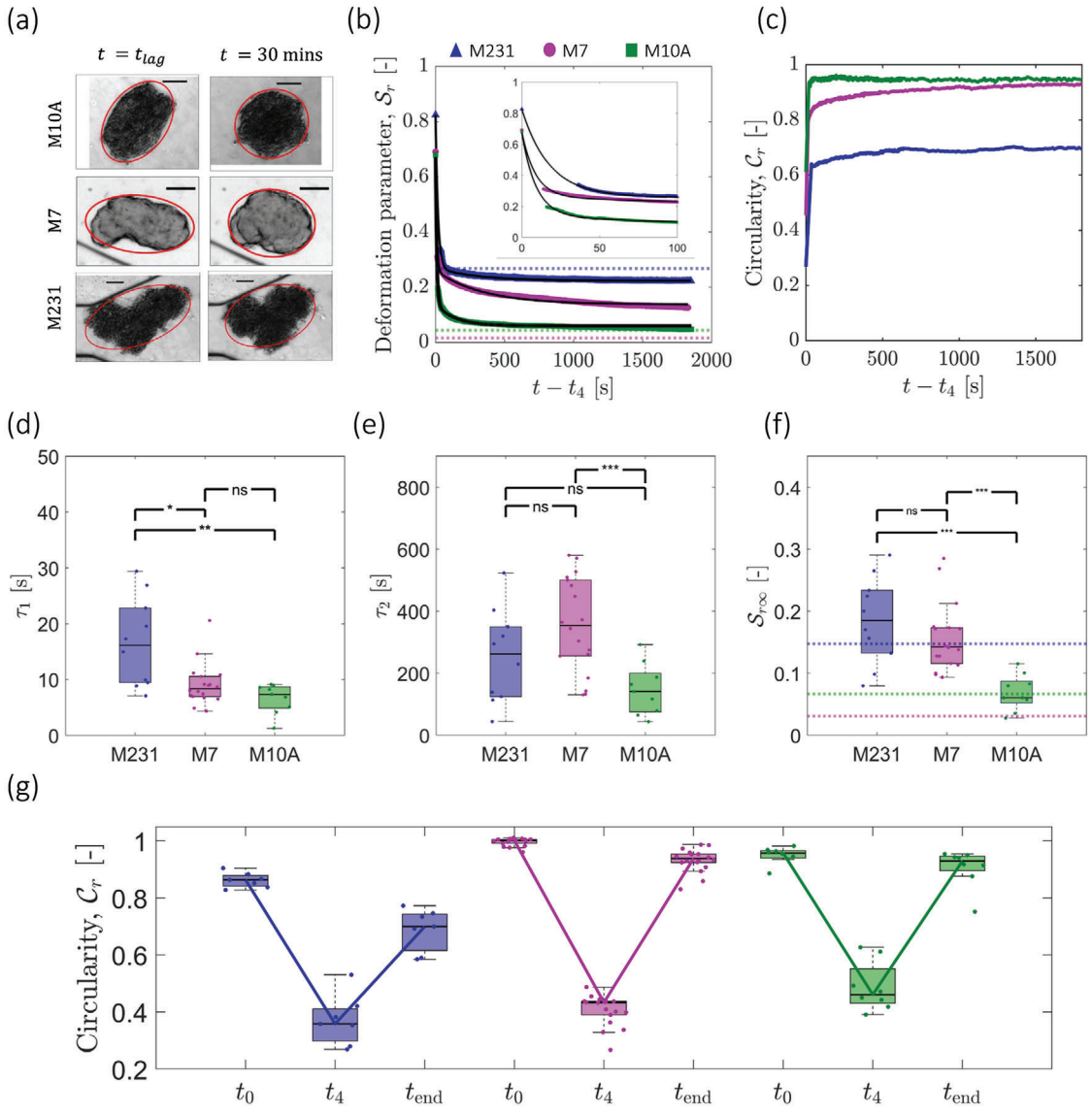

Figure 3. Shape relaxation and recovery of spheroids with different metastatic potential after the dynamic compression ($I_c \geqslant 0.6$). a) Brightfield images of MDA-MB-231, MCF-7 and MCF-10A spheroids in the relaxation stage: images taken at t = tl_{ag}l and after 30 min from the time of maximum compression t_4. b) Deformation parameter $\mathcal{S}_r$ over time and the double exponential model (DEM) fitting. The starting point in each curve is shifted to t_4 and refers to the $\mathcal{S}_r$ value at maximum compression. The dotted lines refer to the deformation parameter of each spheroid prior to compression $\mathcal{S}_{r0}$. The inset shows the fitting of the first 100 s. c) Circularity $\mathcal{C}_r$ curve over time during the relaxation stage. MCF-10A and MCF-7 spheroids recover the circular shape, whereas MDA-MB-231 spheroids maintain an irregular shape after deformation. d) Short (τ_1) e) long (τ_2) timescales of relaxation and f) residual deformation $\mathcal{S}_{r\infty}$ based on the DEM fits for spheroids of $I_c \geqslant 0.6$. The dotted lines in 3f indicate the median values of the deformation parameter prior to compression $\mathcal{S}_{r0}$ (n_{M231}=10), (n_{M7}=18), (n_{M10A}=9). g) Boxplots of circularity $\mathcal{C}_r$ before compression (t_0), at the maximum compression (t_4) and after 30 min of relaxation (t_{end}) for the three spheroid type. The highly metastatic spheroids do not recover their initial circularity values, differently from the less metastatic MCF-7 spheroids and the benign MCF-10A spheroids (n_{M231}=7), (n_{M7}=18), (n_{M10A}=8). Data = solid line in the boxplot is the sample median. Box edges are first and third quartiles (IQR). Whiskers within 1.5 IQR value. The significance was calculated by a two-tailed *t*-test: ns = non significant, $p < 0.001$ (***), $p < 0.01$ (**) and $p < 0.05$ (*).

(MDA-MB-231) spheroids. Notably, both MCF-7 and MCF-10A can be distinguished from highly metastatic MDA-MB-231 spheroids in terms of greater compactness, quantified by their high circularity values ($\mathcal{C}_r \approx 1$) prior to compression (Figure 3g). The absence of inherent cell–cell adhesion in the latter resulted in less spherical MDA-MB-231 spheroids with circularity values ($\mathcal{C}_r \approx 0.85$). To examine this further, we visualize the F-actin distribution within each spheroid prior to compression (**Figure** 4a,b). We observe that both MCF-10A and MCF-7 form compact spheroids distinguished by a peripheral actin rim, which is more pronounced in the benign MCF-10A spheroids. Based on this result, we hypothesize that the fast relaxation (i.e. τ_1) is primarily influenced by surface elasticity resulting from the peripheral distribution of actin fibers, rather than solely by the bulk

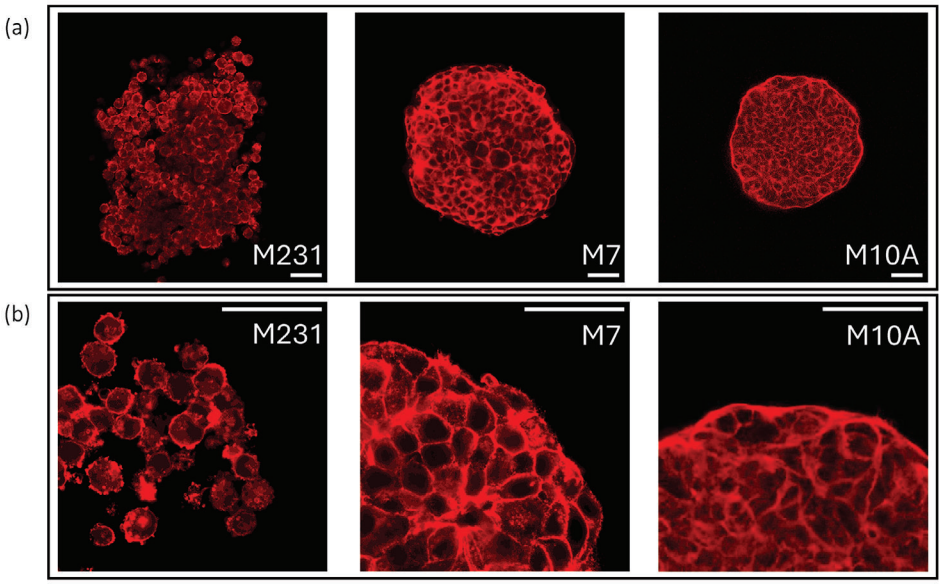

Figure 4. F-actin immunostaining in breast cancer spheroids of different malignancy. a) Confocal images (at 20x) of F-actin (at the equitorial plane) in MDA-MB-231, MCF-7 and MCF-10A breast spheroids (from left to right): MCF-10A spheroids display smooth edges with a prominent collective actin rim, MCF-7 spheroids show similar, but less pronounced, actin rim, while MDA-MB-231 spheroids exhibit fragmented edges lacking a collective actin rim. b) Same spheroids at higher magnification (63x): MCF-10A cells at the boundary display stretched morphology with compact and smooth actin organization. MCF-7 spheroid edges are similarly compacted, but have slightly rougher contours. In contrast, MDA-MB-231 spheroids feature non-interconnected cells with irregular F-actin distribution. Scale bar is 50 μm.

elasticity. This is supported by the significant difference in bulk elastic moduli, yet similar τ_1 values, between MCF-10A and MCF-7. To test this hypothesis, we examined the relaxation behavior of MCF-7 spheroids treated with blebbistatin, an inhibitor of myosin-II-specific ATPase, responsible for decreased actomyosin contractility (see Figure S8a, Supporting Information). The MCF-7 spheroids treated with blebbistatin show different relaxation dynamics compared to untreated cases. In particular, the fast relaxation timescale τ_1 is statistically higher when the actomyosin contractility is inhibited, whereas the longer relaxation timescale τ_2 remains unaltered. Furthermore, the F-actin immunostaining on MCF-7 (+ blebbistatin) spheroids reveals slightly rougher contours suggesting a reduced contractile actin rim compared to the untreated spheroids (see Figure S8b, Supporting Information). In contrast to MCF-7 and MCF-10A, MDA-MB-231 exhibits lower circularity ($C_r \approx 0.85$), lacks a visible F-actin cortex, and thereby displays prolonged initial relaxation and greater variability in the τ_1 values. This suggests that the absence of a structured actin cortex contributes to a more heterogeneous and extended relaxation response in the MDA-MB-231 spheroid (see inset in Figure 3b).

The subsequent slow relaxation is characterized by the longer timescale τ_2, governed by the bulk elasticity (E). Benign spheroids (MCF-10A) exhibit the shortest relaxation time (with $\tau_2 \approx 141$ s), indicative of their higher elasticity and compact structure, enabling quick and uniform relaxation. The two malignant cell lines (MCF-7 and MDA-MB-231) display similar slow relaxation times, but with higher τ_2 compared to MCF-10A. These late-time relaxation timescales are consistent with the E values derived from dynamic compression and deformation, with lower elasticity for the malignant spheroids (MCF-7 and MDA-MB-231) compared to MCF-10A spheroids. The median value of τ_2 for MDA-MB-231 is smaller, yet not statistically different, than for MCF-7. MDA-MB-231 cells form a more compliant and flexible spheroid, with cells at the periphery that are more free to move and rearrange, while MCF-7 spheroids, despite being less metastatic, maintain their deformed state for a longer time, but are still capable to recover most of the spherical initial shape (up to 93.7%), as shown by the circularity plot in Figure 3g.

At the end of 30 min of relaxation, all benign MCF-10A spheroids nearly regain their original deformation S_{r0}, such that $S_{r\infty} \rightarrow S_{r0}$ (Figure 3f). They also achieve a final circularity value nearly identical to their initial shape before compression (retrieving 97% of original circularity), as depicted in Figure 3g. By contrast, the malignant MCF-7 cell lines display much greater resistance to recovery due to long time viscous effects with significant residual deformation ($S_{r\infty}$) at the end of our experimental time. The residual deformation of MDA-MB-231 ($S_{r\infty}$) is found to be case specific due to cell-cell rearrangements, which results in a broad range of $S_{r\infty}$ values both above and below their original deformation parameter (S_{r0}). The two malignant spheroids also differ significantly in their morphological recovery: MCF-7 spheroids regain a spherical shape, while MDA-MB-231 spheroids display fragmented edges, with cells moving in different directions (Movie S2, Supporting Information), leading to an overall irregular spheroid shape.

3. Discussion and Conclusion

In this work, we investigate the relationship between the viscoelastic properties of breast spheroids and their metastatic potential through dynamic compression and relaxation

experiments. We use a microfluidic chip to systematically analyze spheroid deformation and subsequent relaxation, allowing us to obtain the bulk elastic modulus (E) and viscosity (η) through a viscoelastic model tailored to the experimental conditions.

Benign spheroids display higher E and η compared to the low and high metastatic counterparts (MCF-7, MDA-MB-231). These findings on breast cancer spheroids align with previous studies on single breast cancer cells[36,43–45] and on spheroids of different tissues, e.g., originating from bladder cancer.[46] Notably, among the three cell lines, only MCF-10A shows significant sensitivity in both E and η to the imposed maximum strain, with higher values corresponding to increased level of maximum strain. This behavior, also observed on single MCF-10A cells previously,[36] indicates that the apparent viscoelasticity of a spheroid is not only imposed strain-dependent,[47] but also is specific to the spheroid's metastatic potential.

Additionally, the variation in spheroid entry time relative to metastatic potential corroborates earlier findings on single breast cancer cells in a similar constriction channel.[9] The higher entry time for benign MCF-10A cells, compared to MCF-7 and MDA-MB-231, was attributed to their greater stiffness, and correlates with both bulk elasticity and viscosity (Figure S7, Supporting Information). Overall, these studies suggest that malignant breast cancer spheroids, similar to their constituent single cells, are more compliant to deformation compared to healthy spheroids. This translates to a reduced elasticity with higher deformability and reduced viscosity as spheroid's malignancy increases. Tissue fluidity, often considered as the opposite of viscosity, has been defined as an indicator of the invasive potential.[48] Healthy spheroids have immobile, jammed cells, and are characterized by an overall lower fluidity, hence higher viscosity. On the contrary, metastatic spheroids display high cell motility and deformability and a disordered, unjammed state.[49] Such feature corroborates the lower viscosity detected for malignant spheroids in our experiments.

During the relaxation stage we identify two distinct timescales for all three spheroid types. Despite the similarity in the bulk properties of both two malignant spheroids (MCF-7 and MDA-MB-231) during compression, we observe distinct behaviors in their relaxation. The early-time fast relaxation, characterized by smaller τ_1 values, is attributed to surface elasticity. Both MCF-7 and MCF-10A spheroids, with their distinct peripheral actin rims and spherical shape, exhibit a faster initial rebound compared to MDA-MB-231 spheroids. Immunostaining of F-actin fibers reveals that this peripheral actin rim is present in MCF-10A and MCF-7 spheroids, but is absent in MDA-MB-231 spheroids, which exhibit a highly irregular shape, as highlighted in previous studies.[50] This indicates that the structural arrangement of actin fibers significantly influences the early-time relaxation dynamics, (making the less malignant MCF-7 behave more like the benign MCF-10A spheroid than the highly malignant MDA-MB-231 spheroid. We quantify this surface characteristic through spheroid circularity, which is much closer to 1 for MCF-10A ($C_r \approx 0.96$) and MCF-7 ($C_r \approx 1$) than MDA-MB-231 ($C_r \approx 0.86$). The late-time slow relaxation is correlated with the bulk elasticity (E) values with a shorter τ_2 for the benign MCF-10A than the malignant MCF-7. Notably, we do not observe a dominant viscous effect within the experimental time frame of relaxation (30 min), especially for MCF-7 and MCF-10A. Despite MCF-10A spheroids having the highest viscosity among the three types, a longer viscous relaxation timescale is expected, but is not observed in our experiments. The long time viscous effects (beyond experimental time) in MCF-7 spheroids, leading to residual deformation ($S_{r\infty}$) after the dynamic compression stage, may be linked to changes in E-cadherin-mediated adhesions, which are known to either strengthen or weaken under mechanical stress.[51] Additionally, the mechanical compression could also lead to inhomogeneous cellular rearrangements within the spheroid.[24] A future experiment examining the cellular rearrangement and E-cadherin juncture modification within the MCF-7 spheroid would help understand these long-time effects.

Although MDA-MB-231 shows a τ_2 similar to MCF-7, aligning with their respective elastic moduli, we believe that the relaxation of the former is more complex and is likely influenced by the rearrangement of individual cells. The non-uniform actin distribution in MDA-MB-231 spheroids, seen in Figure 4 (also reported earlier in ref. [50, 52]), limits its ability to recover a morphologically compact, circular shape, unlike MCF-7 (see Figures 3g and 4). This has resulted in a broad range of post-relaxation deformation parameter $S_{r\infty}$ in MDA-MB-231 spheroids, including values lower than their pre-compression values (S_{r0}) (see Figure 3b). We hypothesize that, due to the mesenchymal characteristics of this cell line, cells at the periphery of MDA-MB-231 spheroids exhibit increased mobility (Movie S2, Supporting Information), enhancing the potential for cell-cell rearrangements. These rearrangements are facilitated by the lack of E-cadherin expression in the highly metastatic MDA-MB-231 cells, which is crucial for cell–cell adhesion.[53,54] This further contributes to the spheroid's loosening during the dynamic compression stage influencing the cell rearrangement during the relaxation.[55] In a separate experiment, an MDA-MB-231 spheroid subjected to high $I_c = 0.87$ fragments during dynamic compression, with individual cells disseminating from the spheroid (see Movie S3, Supporting Information). This confirms that spheroids with high metastatic potential (with mesenchymal features) are more prone to deforming irreversibly and breaking, disseminating invasive tumor cells under external physical forces (such as compression), due to unstable cell–cell contact and weak cortical contractility.[50]

To summarize, we compare the viscoelastic properties of benign spheroids with malignant spheroids (with low and high metastatic potentials). Notably, the benign spheroids exhibit the highest bulk elasticity, viscosity, and resistance to deformation, in contrast to the two malignant spheroids. We find that both low and high metastatic spheroids have similar apparent viscoelastic properties; however, they differ significantly during the relaxation phase. Important extension of this work could be the investigation of heterogeneous spheroids to mimic the diverse cellular population within the tumor. From a clinical standpoint, the investigation of the mechanical properties of patient derived biopsy samples (from patients diagnosed by breast cancer) would allow to link them to different stages of metastasis. The microfluidic platform developed in this work provides mechanistic insights into physiological processes, such as cellular remodeling within invasive tumors, and identifies unique "mechanical biomarkers." These biomarkers can be applied in developing therapeutic approaches that target the dissemination of primary solid tumors.[5,6]

4. Experimental Section

Cell Culture and Spheroid Formation: Human mammary MCF-10A cells (ATCC CRL-10317) were cultured in DMEM/F12 1:1 medium (Gibco) supplemented with 5% horse serum (Gibco), 0.5 µg mL^{-1} hydrocortisone (Sigma), 20 ng mL^{-1} human epidermal growth factor (hEGF) (Peprotech), 100 ng mL^{-1} cholera toxin (Sigma), 10 g mL^{-1} insulin (Human Recombinant Zinc, Gibco) and 1% Penicillin–Streptomycin 100× solution (VWR Life Science). Human mammary MCF-7 mCherry cells and MDA-MB-231 LifeAct GFP (kindly provided by Peter ten Dijke's lab) were cultured in DMEM medium (Gibco) supplemented with 5% fetal bovine serum (Gibco) and 1% antibiotic-antimycotic solution (Gibco). All cells were incubated at 37 °C with 5% CO_2 and subcultured at least twice a week. Cells were regularly tested for absence of mycoplasma. Spheroids were formed in a commercially available Corning Elplasia 96-well plate or Sphericallate 5D (Kugelmeiers) designed for efficient spheroid production. These plates have a round-bottom shape and a specialized Ultra-Low Attachment (ULA) surface that prevents cells from attaching to the plate and encourages cell-to-cell adhesion. The size of the spheroids depends on factors such as the initial seeding density and the duration of the culture (related to proliferation rate of each cell line). The seeding density was tuned to obtain a spheroid diameter of 200–220 µm after 2 days of culture in the case of MCF-7 and MCF-10A. Due to the lack of cell–cell adhesion (E-cadherin), the MDA-MB-231 spheroids required a separate protocol compared to the other two cells. To promote cell adhesion and spheroid formation for MDA-MB-231 cells, the media was supplemented with methylcellulose (Merck Sigma) in a ratio of 1:4 to promote spheroid compactness.[56,57] The spheroids were harvested after 5 days. After harvesting, MDA-MB-231 spheroids were resuspended in methylcellulose-free media to ensure the same media viscosity across the three cell lines. It was verified that the addition of methylcellulose did not affect the viscoelastic properties using a separate experiment (see Figure S9, Supporting Information).

Blebbistatin Treatment: Myosin II inhibitor (-) Blebbistatin (ab120425) was dissolved in dimethyl sulfoxide (DMSO) at a stock concentration of 5 mM. Spheroids were treated with 10 µM blebbistatin for 3 h before experiments.

Spheroids Fixation, Permeabilization, Immunostaining, and Imaging: Spheroids were fixed with 4% paraformaldehyde for 30 min at room temperature (RT) and then permeabilized using 0.1% Triton X-100 (diluted in PBS) at RT for 5 min. For immunostaining, cells were incubated with Phalloidin iFluor 647 Reagent (ab176759) diluted 1:100 in 1% bovine serum albumin (BSA) for 90 min at RT. In between all steps, the samples were washed multiple times using PBS. Samples were kept at 4 °C, protected from light. Soon after the staining procedure, the spheroids were placed in uncoated chamber wells (ibidi) for visualization of the F-actin organization. Images were acquired on a confocal microscope (LSM 980 with Airyscan 2, Zeiss) equipped with Plan Apochromat 20x/0.8 M27 air objective (to image the whole spheroid) and Plan Apochromat 63x/1.40 Oil DIC M27 objective for the spheroids' edges ($\lambda_{ex} = 653$ nm and $\lambda_{em} = 668$ nm). Z-stacks were acquired with a step of 5 µm and the equitorial planes were chosen for the visualization of the whole spheroids and their edges. Images post-processing was performed on ImageJ (v1.53t, National Institute of Health, USA).

Microfluidic Chip Design and Experimental Setup: A 4-inch silicon wafer was used as the base material for the chip, and the fabrication process was carried out in a cleanroom facility (Kavli Nanolab Delft) via a photo-lithography process using the µMLA Laser Writer (Heidelberg Instruments). A detailed procedure of the wafer fabrication can be found in the Supporting Information. Using the master mold as a template, the microfluidic chips were then produced using the soft lithography technique with polydimethylsiloxane (PDMS) as the main material.The day before each experiment, the chips were coated with 1% BSA (Sigma Aldrich) in DPBS buffer solution to reduce friction of the spheroids with the channel walls. The chips were kept overnight at 37 °C and with sufficient humidity. The day of the experiment the chips were flushed with DPBS to remove BSA extra residues and eventual dirt. The three serpentines positioned at the inlet allow for the stabilization of the flow when the spheroid enters the chip, whereas the last serpentine is strategically utilized to impede the spheroid's exit, ensuring its prolonged residence in the relaxation chamber. The height of the chip (180 ± 15 µm) is uniform along the whole design. To prevent the tumbling of the spheroids, spheroids were selected with a higher diameter than the height of the chip. This allows for a pre-compression of the spheroid in the z-axis, enabling subsequent observations and measurements to be conducted within the recording x-y plane. This also implies the clogging of the flow when the spheroids enter the constriction, excluding possibilities of shear flow between the spheroids and the channel walls. The microfluidic chips have been fabricated with different constriction widths (60–65 µm, 84–94 µm and 100–110 µm). The experimental setup consists of a 200 µL pipette tip plugged into the inlet for the spheroids loading, while at the outlet a tube is connected to an In-Line pressure sensor, S version (Fluigent) for a continuous measurement of pressure. Additionally, a syringe pump (Harvard Apparatus, Pump 11 Pico Plus Elite) operating in withdrawal mode (4 µL min^{-1}) is used to ensure constant fluid flow and enable the spheroids to pass through the constriction in a controlled manner. When the spheroid exits the constriction the withdrawal flow rate is immediately set to zero, allowing to keep the spheroid within the relaxation chamber. The spheroids are individually loaded into the pipette tip at the inlet, together with the cell culture media, one at a time, to prevent flow and pressure instability given by the traverse of two or more spheroids in the microfluidic chip. Experiments that had more than one spheroid flowing in the chip were not considered in the analysis. All experiments were conducted at 37 °C through a Heating Insert (ibidi). The inlet reservoir precluded the use of a lid for humidity and CO_2 control.

Data Acquisition and Analysis: Brightfield images of the spheroids entering the constricted channels were captured on an inverted fluorescence microscope (Zeiss Axio-Observer) with camera streaming (for the compression stage) using a 5×/NA 0.16 air objective and Zeiss Axio-Observer 0.63x digital camera with a resolution of 2048x2048 μm^2. Once the spheroid exited the constriction, the syringe pump was paused to allow the spheroid to reside in the chamber. For the relaxation phase, images were taken at 2 fps for the first 10 min, and successively at 0.1 fps for the remaining 20 min, for a total of 30 min of relaxation recording in the same imaging conditions as during the compression. To analyze the dynamic compression data, an image without the spheroid was subtracted from the image containing the spheroid to remove all background noise and identify the spheroid contour (edges in red in Figure 1b). The image was then converted to binary format, and morphological closing was applied to remove the rough edges from the boundary of the spheroid. To determine the spheroid axial dimensions prior to (D_0) and during compression (D(t)), a MATLAB function that detects the minimum and maximum pixel values in the horizontal direction was used. The velocity (u_s) of the spheroid was calculated by first identifying the centroid (using regionprops function in MATLAB) and then averaging the displacements of the centroid for consecutive images according to the Δt from one image to the other. For the relaxation, given the variable orientation of the spheroid in the relaxation chamber, it was not possible to implement the same function used for the dynamic compression to detect the length of the deformed spheroid. Therefore, an ellipse fitting was used and its major and minor axes (white lines in Figure 1c) were detected to calculate the deformation parameter $\mathcal{S}_r$.

Pressure Characterization and D3M Model: The spheroid entering the constriction clogged the fluid flow, causing the volumetric flow rate in the channel to go to zero. However, the withdrawal force applied by the syringe pump remained constant, causing an increase in the pressure in the constriction, detected by the pressure sensor located at the outlet. The sensor recorded a linear pressure increase, meaning that the stress experienced by the spheroid linearly increased during the compression phase (Figure 2a). The deformation of the spheroid in the main constriction is fitted by the Dynamic Modified Maxwell Model (D3M), up to the inflex point of the strain curve, corresponding to the time t_2. The model considers the pressure as an affine line, rather than a constant value as the Modified Maxwell Model (MMM), used for conventional MPA experiments. The two models share the same schematic, but the governing equations are different because of the time dependence of the pressure.

The general governing equation is given by (for full derivation refer to Supporting Information):

$$\ddot{\varepsilon} + \frac{\dot{\epsilon}}{\tau_c} = (\frac{1}{E\tau_c} + \frac{1}{\eta})\dot{\sigma} + \frac{1}{\eta\tau_c}\sigma \tag{4}$$

with $\tau_c = \frac{\eta^*(E^*+E)}{E^*E}$

The initial conditions for the stress and strain are the following:

$$\sigma(0) = \Delta P_0 \tag{5}$$

$$\dot{\sigma}(0) = \Delta \dot{P} \tag{6}$$

$$\epsilon(0) = \frac{\Delta P_0}{E^* + E} \tag{7}$$

$$\dot{\epsilon}(0) = \frac{\Delta \dot{P}}{E^* + E} + \frac{E^{*2}\Delta P_0}{\eta^*(E^* + E)^2} + \frac{\Delta P_0}{\eta} \tag{8}$$

The resolution of the differential equation gives us:

$$\dot{\epsilon}(t) = \frac{\Delta P_0}{\tau_c}\frac{e^{-\frac{t}{\tau_c}}}{E_{(1,2)}} + \frac{\Delta \dot{P}t + \Delta P_0}{E} \tag{9}$$

with $E_{(1,2)} = \frac{E_2(E_1+E_2)}{E_1}$

Statistical Analysis: The solid line in the boxplots represents the median value. The box edges indicate the interquartile range (IQR), spanning from the 25*th* percentile (Q_1) to the 75*th* percentile (Q_3). The dotted whiskers are within 1.5 times the IQR from the quartile. Outliers are represented by individual markers outside the dotted whiskers range. All statistical analysis was performed using Microsoft Excel (Microsoft Corporation, USA) and MATLAB. The statistical significant differences between the experimental groups were determined by Student *t*-test using the function *t*-test: two-tailed distribution with unequal variance and p values below 0.05 were considered to be significant. Statistical differences were categorized as following: $p < 0.001$ (***), $p < 0.01$ (**) and $p < 0.05$ (*).

Supporting Information

Supporting Information is available from the Wiley Online Library or from the author.

Acknowledgements

The authors thank Peter ten Dijke (from Leiden University Medical Center) for kindly providing MCF-7 mCherry and MDA-MB-231 LifeAct GFP cells. M.T. and P.E.B. gratefully acknowledge funding from the European Research Council (ERC) under the European Union's Horizon 2020 research and innovation program (grant agreement no. 819424). A.D.B. gratefully acknowledges funding from MSCA Postdoctoral Fellowships 2022 Project ID: 101111247. E.T. was supported by an Erasmus+ Traineeship.

Conflict of Interest

The authors declare no conflict of interest.

Author Contributions

M.T., A.D.B., and P.E.B. conceived the ideas and designed the experiments. M.T., E.T., and S.D. carried out the experiments and collected the data. M.T. and A.D.B. performed data and image analysis. A.D.B. developed MATLAB codes for image analysis. E.T., A.D.B., and M.T. developed the model. M.T. wrote the paper and A.D.B., V.G., and P.E.B. edited it.

Data Availability Statement

The data that support the findings of this study are available from the corresponding author upon reasonable request.

Keywords

deformation and relaxation, microfluidics, malignancy, spheroid viscoelasticity, tissue mechanics

Received: July 23, 2024
Revised: September 13, 2024
Published online:

[1] D. Wirtz, K. Konstantopoulos, P. C. Searson, *Nat. Rev. Cancer* **2011**, *11*, 512.
[2] E. Cambria, M. F. Coughlin, M. A. Floryan, G. S. Offeddu, S. E. Shelton, R. D. Kamm, *Nat. Rev. Cancer* **2024**, *24*, 216.
[3] H. T. Nia, L. L. Munn, R. K. Jain, *Science* **2020**, *370*, eaaz0868.
[4] V. Gensbittel, M. Kräter, S. Harlepp, I. Busnelli, J. Guck, J. G. Goetz, *Dev. Cell* **2021**, *56*, 164.
[5] A. Massey, J. Stewart, C. Smith, C. Parvini, M. McCormick, K. Do, A. X. Cartagena-Rivera, *Nat. Rev. Phys.* **2024**, *6*, 269.
[6] W. Yu, S. Sharma, E. Rao, A. C. Rowat, J. K. Gimzewski, D. Han, J. Rao, *J. Natl. Cancer Cent.* **2022**, *2*, 10.
[7] S. E. Cross, Y. S. Jin, J. Rao, J. K. Gimzewski, *Nat. Nanotechnol.* **2007**, *2*, 780.
[8] C. Rianna, M. Radmacher, S. Kumar, *Mol. Biol. Cell* **2020**, *31*, 1726.
[9] H. W. Hou, Q. S. Li, G. Y. Lee, A. P. Kumar, C. N. Ong, C. T. Lim, *Biomed. Microdevices* **2009**, *11*, 557.
[10] H. A. Cognart, J. L. Viovy, C. Villard, *Sci. Rep.* **2020**, *10*, 1.
[11] Z. Yan, X. Xia, W. C. Cho, D. W. Au, X. Shao, C. Fang, Y. Tian, Y. Lin, *Adv. Healthcare Mater.* **2022**, *11*, 8.
[12] P. Shah, C. M. Hobson, S. Cheng, M. J. Colville, M. J. Paszek, R. Superfine, J. Lammerding, *Curr. Biol.* **2021**, *31*, 753.
[13] T. Fuhs, F. Wetzel, A. W. Fritsch, X. Li, R. Stange, S. Pawlizak, T. R. Kießling, E. Morawetz, S. Grosser, F. Sauer, J. Lippoldt, F. Renner, S. Friebe, M. Zink, K. Bendrat, J. Braun, M. H. Oktay, J. Condeelis, S. Briest, B. Wolf, L. C. Horn, M. Höckel, B. Aktas, M. C. Marchetti, M. L. Manning, A. Niendorf, D. Bi, J. A. Käs, *Nat. Phys.* **2022**, *18*, 1510.
[14] N. V. Popova, M. Jücker, *Cancers* **2022**, *14*, 238.
[15] A. Elosegui-Artola, A. Gupta, A. J. Najibi, B. R. Seo, R. Garry, C. M. Tringides, I. de Lázaro, M. Darnell, W. Gu, Q. Zhou, D. A. Weitz, L. Mahadevan, D. J. Mooney, *Nat. Mater.* **2023**, *22*, 117.
[16] A. Aung, S. K. Davey, J. Theprungsirikul, V. Kumar, S. Varghese, *Adv. Healthcare Mater.* **2022**.
[17] W. Kang, J. Ferruzzi, C.-P. Spatarelu, Y. L. Han, Y. Sharma, S. A. Koehler, J. A. Mitchel, A. Khan, J. P. Butler, D. Roblyer, M. H. Zaman, J.-A. Park, M. Guo, Z. Chen, A. F. Pegoraro, J. J. Fredberg, *iScience* **2021**, *24*, 11.
[18] K. S. Kopanska, Y. Alcheikh, R. Staneva, D. Vignjevic, T. Betz, *PLoS ONE* **2016**, *11*, 6.
[19] M. Kalli, T. Stylianopoulos, *Front Oncol.* **2018**.
[20] Z. Rahman, A. D. Bordoloi, H. Rouhana, M. Tavasso, G. van der Zon, V. Garbin, P. ten Dijke, P. E. Boukany, *Lab on a Chip* **2023**.
[21] K. Jiang, L. Liang, C. T. Lim, iScience Engineering confining microenvironment for studying cancer metastasis.
[22] R. C. Boot, A. Roscani, L. van Buren, S. Maity, G. H. Koenderink, P. E. Boukany, *Lab on a Chip* **2023**.
[23] S. L. Tlili, F. Graner, H. Delanoë-Ayari, *Development* **2022**, *149*, 20.
[24] S. Jain, H. Belkadi, A. Michaut, S. Sart, J. Gros, M. Genet, C. N. Baroud, *Biofabrication* **2024**, *16*, 3.

[25] I. Pajic-Lijakovic, in *Viscoelasticity and Collective Cell Migration: An Interdisciplinary Perspective Across Levels of Organization*, Elsevier, Amsterdam **2021**, pp. 21–46.
[26] G. S. Oostenbrug, R. P. Mensink, M. R. Hardeman, T. De Vries, F. Brouns, G. Hornstra, *J. Appl. Physiol.* **1997**, *83*, 746.
[27] D. Bento, R. O. Rodrigues, V. Faustino, D. Pinho, C. S. Fernandes, A. I. Pereira, V. Garcia, J. M. Miranda, R. Lima, *Micromachines* **2018**, *9*, 151.
[28] K. Matthews, E. S. Lamoureux, M. E. Myrand-Lapierre, S. P. Duffy, H. Ma, *Lab Chip.* **2022**.
[29] K. Guevorkian, M. J. Colbert, M. Durth, S. Dufour, F. Brochard-Wyart, *Phys. Rev. Lett.* **2010**, *104*, 21.
[30] K. Guevorkian, D. Gonzalez-Rodriguez, C. Carlier, S. Dufour, F. Brochard-Wyart, *PNAS* **2011**, *108*, 13387.
[31] K. Guevorkian, F. Brochard-Wyart, D. Gonzalez-Rodriguez, in *Viscoelasticity and Collective Cell Migration: An Interdisciplinary Perspective Across Levels of Organization*, Elsevier, Amsterdam **2021**, pp. 193–223.
[32] M. Yu, A. Mahtabfar, P. Beelen, Y. Demiryurek, D. I. Shreiber, J. D. Zahn, R. A. Foty, L. Liu, H. Lin, *Biophys. J.* **2018**, *114*, 2703.
[33] P. Marmottant, A. Mgharbel, J. Kä Fer, B. Audren, J.-P. Rieu, J.-C. Vial, B. Van Der Sanden, A. F. M. Maré E D, F. Graner, H. Lè Ne Delanoë Ayari, Technical report, www.pnas.org/cgi/content/full/.
[34] R. Ferraro, S. Caserta, S. Guido, *Adv. Mater. Technol.* **2024**, *9*, 4.
[35] X. Xie, F. Sauer, S. Grosser, J. Lippoldt, E. Warmt, A. Das, D. Bi, T. Fuhs, J. A. Käs, *Soft Matter* **2024**, *20*, 1996.
[36] Q. S. Li, G. Y. Lee, C. N. Ong, C. T. Lim, *Biochem. Biophys. Res. Commun.* **2008**, *374*, 609.
[37] B. Zbiral, A. Weber, M. d. Vivanco, J. L. Toca-Herrera, *Int. J. Mol. Sci.* **2023**, *24*, 15.
[38] S. Moreno-Flores, R. Benitez, M. D. Vivanco, J. L. Toca-Herrera, *Nanotechnology* **2010**, *21*, 44.
[39] G. Forgacs, R. A. Foty, Y. Shafrir, M. S. Steinberg, *Biophys. J.* **1998**, *74*, 2227.
[40] K. Jakab, B. Damon, F. Marga, O. Doaga, V. Mironov, I. Kosztin, R. Markwald, G. Forgacs, *Developmental Dynamics* **2008**, *237*, 2438.
[41] M. Layachi, L. Casas-Ferrer, G. Massiera, L. Casanellas, *Front. Phys.* **2022**, *10*.
[42] N. Khalilgharibi, J. Fouchard, N. Asadipour, R. Barrientos, M. Duda, A. Bonfanti, A. Yonis, A. Harris, P. Mosaffa, Y. Fujita, A. Kabla, Y. Mao, B. Baum, J. J. Muñoz, M. Miodownik, G. Charras, *Nat. Phys.* **2019**, *15*, 839.
[43] M. Dessard, J. B. Manneville, J. F. Berret, *Nanoscale Adv.* **2024**, *6*, 1727.
[44] M. Nikkhah, J. S. Strobl, R. De Vita, M. Agah, *Biomaterials* **2010**, *31*, 4552.
[45] C. Alibert, B. Goud, J. B. Manneville, *Biol. Cell.* **2017**.
[46] K. Gnanachandran, S. Kędracka-Krok, J. Pabijan, M. Lekka, *J. Biomech.* **2022**, *144*.
[47] R. C. Boot, A. van der Net, C. Gogou, P. Mehta, D. H. Meijer, G. H. Koenderink, P. E. Boukany, *Sci Rep.* **2024**, *14*, 20013.
[48] F. Sauer, S. Grosser, M. Shahryari, A. Hayn, J. Guo, J. Braun, S. Briest, B. Wolf, B. Aktas, L. C. Horn, I. Sack, J. A. Käs, *Adv. Sci.* **2023**, *10*, 26.
[49] S. Grosser, J. Lippoldt, L. Oswald, M. Merkel, D. M. Sussman, F. Renner, P. Gottheil, E. W. Morawetz, T. Fuhs, X. Xie, S. Pawlizak, A. W. Fritsch, B. Wolf, L. C. Horn, S. Briest, B. Aktas, M. L. Manning, J. A. Kas, *Phys. Rev. X* **2021**, *11*, 1.
[50] E. Warmt, S. Grosser, E. Blauth, X. Xie, H. Kubitschke, R. Stange, F. Sauer, J. Schnauß, J. M. Tomm, M. Von Bergen, J. A. Kas, *New J. Phys.* **2021**, *23*, 10.
[51] K. V. Iyer, R. Piscitello-Gómez, J. Paijmans, F. Jülicher, S. Eaton, *Curr. Biol.* **2019**, *29*, 578.
[52] M. Zanetti, L. Andolfi, M. R. Taylor, L. Mestroni, M. Lazzarino, *Micro and Nano Engineering* **2022**, *15*.
[53] A. Ivascu, M. Kubbies, *Int. J. Oncol.* **2007**, *31*, 1403.
[54] G. C. Russo, A. J. Crawford, D. Clark, J. Cui, R. Carney, M. N. Karl, B. Su, B. Starich, T. S. Lih, P. Kamat, Q. Zhang, P. R. Nair, P. H. Wu, M. H. Lee, H. S. Leong, H. Zhang, V. W. Rebecca, D. Wirtz, *Oncogene* **2024**, *43*, 1445.
[55] M. Pandey, Y. J. Suh, M. Kim, H. J. Davis, J. E. Segall, M. Wu, *Phys. Biol.* **2024**, *21*.
[56] H. P. Naber, E. Wiercinska, P. T. Dijke, T. van Laar, *J. Visual. Exper.* **2011**, 57.
[57] B. M. Leung, S. C. Lesher-Perez, T. Matsuoka, C. Moraes, S. Takayama, *Biomater. Sci.* **2015**, *3*, 336.